Nonlinear Elastic Registration of Brain Images with Tumor Pathology Using a Biomechanical Model

Stelios K. Kyriacou,* Christos Davatzikos, S. James Zinreich, and R. Nick Bryan

***Abstract*— A biomechanical model of the brain is presented, using a finite-element formulation. Emphasis is given to the modeling of the soft-tissue deformations induced by the growth of tumors and its application to the registration of anatomical atlases, with images from patients presenting such pathologies. First, an estimate of the anatomy prior to the tumor growth is obtained through a simulated biomechanical contraction of the tumor region. Then a normal-to-normal atlas registration to this estimated pre-tumor anatomy is applied. Finally, the deformation from the tumor-growth model is applied to the resultant registered atlas, producing an atlas that has been deformed to fully register to the patient images. The process of tumor growth is simulated in a nonlinear optimization framework, which is driven by anatomical features such as boundaries of brain structures. The deformation of the surrounding tissue is estimated using a nonlinear elastic model of soft tissue under the boundary conditions imposed by the skull, ventricles, and the falx and tentorium. A preliminary two-dimensional (2-D) implementation is presented in this paper, and tested on both simulated and patient data. One of the long-term goals of this work is to use anatomical brain atlases to estimate the locations of important brain structures in the brain and to use these estimates in presurgical and radiosurgical planning systems.**

***Index Terms*— Brain atlas, biomechanics, finite elements, inverse methods, registration, surgical planning.**

I. Introduction

MUCH attention has been given by the medical imaging community to the modeling of normal brain anatomy. Among others, applications of anatomical modeling include computational neuroanatomy [1]–[3], surgical-path planning [4], and virtual medical environments [5]. However, little attention has been given to modeling anatomical abnormalities. In this work we describe steps toward the development of a system which simulates soft-tissue deformation in the brain, caused by the growth of tumors. The main application of our work is currently in the nonrigid matching of brain atlases to brains with pathologies, for the purposes of pre-operative planning. In particular, brain atlases can provide a wealth of information on the structural and functional organization of the brain and, ultimately, on the response of different brain regions to therapeutic procedures, such as radiotherapy. Since they are derived from normal brains, however, brain atlases must be adapted to the pathology of each individual brain. This necessitates the development of a realistic model for tissue deformation due to the growth of a tumor.

Besides the problem of atlas matching, modeling tissue deformation finds application in other areas, including the prediction of intra-operative shift of brain tissue caused by surgical instruments. In particular, the craniotomy and the manipulation of brain tissue with a surgical instrument changes the structure of the brain, often substantially [6]–[8]. Consequently, the pre-operatively-acquired images no longer correspond to reality. This is currently a very important limitation in using preoperative images to navigate through the patient's anatomy. Finally, modeling soft-tissue deformation is a key issue in real-time simulation of neurosurgical manipulations [9]. For example, craniotomy could result in bulging of the cerebral tissue out of the skull opening due to gravity or due to high intracranial pressures. These simulations may be used for both pre-operative planning as well as training.

Most of the brain mechanics literature starts in the late 1960's, when a large study was initiated by the National Institute of Neurological Disorders and Stroke. Mechanical properties of the different brain structures were experimentally investigated and brain mechanics simulations of various complexities were performed. The primary objective for most of that work was the investigation of traumatic brain injury (often due to automobile accidents). Accordingly, most investigators used dynamics rather than statics in their models. In addition, the elastic and failure properties of the tissue were examined. Notable is the work by Metz *et al.* [10], in which experiments were performed on monkey brain tissue under live, fresh, and fixed conditions. Their experiment consisted of inflating a balloon inserted into the brain tissue and monitoring the volume increase in the balloon versus the balloon pressure. They then calculated the Young's modulus of the brain tissue, assuming both linear strain as well as linear elastic material behavior. They found that the Young's modulus ranged between 10 and 35 kPa (1.0E5 - 3.5E5 dyn/cm^2).

Atluri *et al.* [11] looked at the functional and mechanical failure properties of the brain tissue. They performed experiments on 15 Rhesus monkeys with blunt indentation of the pia-arachnoid. Correlation with a finite-element model showed darkened neurons (stained with Verhoeff Van Giesen) when normal strain was approximately 0.2–0.4. It is unfortunate that their work was not followed up with further

Manuscript received November 7, 1997; revised June 21, 1999. This work was supported in part by a grant from the American Cancer Society and in part by ISG Technologies, Toronto, Canada, a grant from the Whitaker Foundation, and by the NIH under Grant R01 AG14971–0251. The Associate Editor responsible for coordinating the review of this paper and recommending its publication was J. Duncan. *Asterisk indicates corresponding author.*

*S. K. Kyriacou, C. Davatzikos, and S. J. Zinreich are with the Neuroimaging Laboratory, Department of Radiology, The Johns Hopkins University School of Medicine, Baltimore, MD 21287 USA.

R. N. Bryan is with the Diagnostic Radiology/Clinical Center, NIH, Bethesda, MD 20892 USA.

Publisher Item Identifier S 0278-0062(99)07427-3.

experimentation/simulations, as this study is one of the few to combine experiment and computations to predict tissue failure.

More recently, a 1994 symposium in Washington, DC, primarily organized by the National Highway Traffic Safety Administration (NHTSA), was instrumental in keeping the subject of brain biomechanics, and, in particular, traumatic brain injury at the forefront of research. In this symposium, many investigators presented, among other topics, two-dimensional (2-D) and three-dimensional (3-D) finite-element models of brain dynamics (see for example, Bandak *et al.* [12] and other references in the same issue).

In the area of quasistatic (i.e., slow enough deformations so that acceleration terms in the equilibrium equations are negligible) brain mechanics, Nagashima and coworkers [13]–[17] used a 2-D finite-element analysis combined with poroelastic theory to model the movement of fluids through the brain. They included the hydraulic conductivity, metabolic water production, hydrostatic pressure, cerebrospinal fluid (CSF) absorption, and mechanical deformation to account for edema and CSF circulation. They used a linear material and linear strains for the elastic deformations. According to the authors, the predicted edema and brain midline shift seemed to correlate well with experiments they performed.

Neff and coworkers [18] used similar 2-D analyses to investigate hydrocephalus, using a commercial finite-element platform. Although they used a linear elastic material model, they did allow for nonlinear strain (large deformation). According to the authors, the essential features of ventricular expansion were well reproduced qualitatively.

Takizawa *et al.* [19] performed 2-D finite-element analysis of an intracranial hematoma. They based their finite-element domain on part of a representative brain slice that contained a single cerebral hemisphere with white and gray matter delineated. Five types of lenticular nucleus (putaminal) hemorrhages were modeled and the tissue stress was correlated with the extent of tissue destruction. They used linear elastic theory, with a nearly incompressible tissue (Poisson's ratio of 0.47) and Young's modulus of approximately 8, 4, and 100 kPa for gray matter, white matter and falx, respectively. However, the authors did not discuss the limitations of using a linear theory in a rather highly nonlinear problem, or the problems that might arise with excessive element distortion due to the very large displacements next to the hemorrhage region.

Wasserman *et al.* [20] applied the finite-element method in a 2-D setting to predict the growth of the tumor under anatomical constraints (e.g., the falx). The authors used a linear material but included nonlinearities, due to the large tissue displacements (nonlinear geometry). According to the authors, their simulations produced visually consistent tumors.

Our work differs from that of other researchers in the following two respects: 1) we use nonlinear elastic material properties as well as nonlinear geometry and 2) we apply the resulting tissue deformation, due to tumor growth, to the registration of MR or CT images to brain atlases. Here, we develop a method for simulating quasistatic brain mechanics, specifically investigating the growth of a brain tumor and the resulting brain deformations. Our goal is to manipulate brain atlases, which are based on normal subjects, by accounting for structural changes occurring with tumor growth, in order to use them as tools in pre-surgical planning or in radiosurgical-plan optimization. The organization of the paper is as follows. Section II contains the techniques used for the finite-element mesh creation, as well as the specifics of the material model used. In addition, our method for the normalization of the tumor image is described in detail. Section III contains various experimental results, as well as some performance tests for our method. Finally, the validity of various assumptions and plans for future work are discussed in Section IV.

II. Methods

We use the finite-element method [21] to accommodate the complexity of the brain anatomy and its inhomogeneous material properties. There is no doubt that the problem we address herein is by nature 3-D and must be treated as such. However, in this paper we present the principles of our approach in 2-D, by considering individual cross-sectional images, primarily because it substantially reduces the computational requirements. The concepts of our work can be extended to 3-D. However, several implementation difficulties need to be overcome in such extension, which are related to excessive computational requirements, mesh generation, and visualization.

In order to develop our 2-D model we have relied on certain approximations. In particular, we use plain stress, i.e., we assume that there is zero stress in the direction normal to our section and use linear triangular elements. In effect, plain stress requires that the material is free to expand along the third direction.

Our model incorporates the parenchyma, the dura and falx membranes, and the ventricles. Some knowledge of the mechanics of the brain is needed before the finite-element method can be used, in particular, the constitutive models [22] and parameters, i.e., the equations that link stresses with strains and the geometry and boundary conditions.

A. Constitutive Models and Parameters

An accurate simulation of the behavior of the brain tissue is, in general, quite difficult due to inter-individual variability and the variation of tissue properties throughout the brain. For simplicity, in this paper we assume that the white matter, the gray matter, and the tumor tissue are nonlinear elastic solids obeying the equations of an incompressible nonlinearly elastic neo-Hookean model. It is customary in tissue mechanics to assume incompressibility since tissues can be easily distorted, but sustain high pressures without significant change of volume. A neo-Hookean material model is often used in the rubber mechanics and may be considered as a very simple form of nonlinear material, since it has only one material constant. A simple extension of the neo-Hookean material, the so-called Mooney–Rivlin material (plus a viscous component), having two constants instead of one, has recently been used by Mendis *et al.* [23] and others.

One way to characterize the mechanical behavior of a material is through the strain energy function w which gives the amount of strain energy per unit of undeformed volume

of material. The strain energy is a function of the deformation field applied. For example, the neo-Hookean material w is

$$w = \mu(I_1 - 3) \tag{1}$$

where μ is the material constant and I_1 is

$$I_1 = \text{tr}\, \boldsymbol{C} \tag{2}$$

where $\boldsymbol{C}$ is the right Cauchy–Green strain tensor [24]. Note that under a coordinate system that is based on the principal directions, $\boldsymbol{C}$ may be written as

$$\boldsymbol{C} = \begin{bmatrix} \lambda_1^2 & 0 & 0 \\ 0 & \lambda_2^2 & 0 \\ 0 & 0 & \lambda_3^2 \end{bmatrix} \tag{3}$$

where $\lambda_i, i = 1,2,3$ are the three principle stretches, i.e., the ratio of final length L over the original length L_o

$$\lambda = \frac{L}{L_o}. \tag{4}$$

Thus,

$$I_1 = \lambda_1^2 + \lambda_2^2 + \lambda_3^2. \tag{5}$$

We will also be using the term strain e to denote the amount of expansion or contraction we apply to the tumor area. This strain is the classical strain, i.e., the ratio of the change in length over the original length and, by definition, it is equal to the stretch minus one

$$e = \frac{L - L_o}{L_o} = \lambda - 1. \tag{6}$$

To illustrate the physical interpretation of $\boldsymbol{C}$, consider uniaxial extension in a standard tensile test where a homogeneous isotropic cylindrical specimen is pulled at its two ends and the deformed length, as well as the change in the diameter, is recorded. In that case, the principal directions for the strain are along the axis of the tensile force and any two axes normal to it. The principal stretch λ_1 along the first axis will be the ratio of the deformed length of the specimen to the undeformed length. The other two principal stretches, λ_2 and λ_3, will be equal and their value will be the ratio of the deformed diameter divided by the undeformed one.

Choosing an appropriate value for μ is an important, but difficult issue. Following the experiments by Metz *et al.* [10], which were discussed in Section I, we use a Young's modulus equal to 18 kPa for the white matter that corresponds to $\mu = 3$ kPa for relatively small values of strain [23]. Since the gray matter has been reported to be approximately ten times stiffer than the white matter [17], we use 30 kPa for the gray matter μ. Tumor tissue is also given the properties of gray matter. An exception is the example of Fig. 8, where we use the same value for the gray matter and tumor μ as the one for the white matter, since one cannot reliably distinguish gray from white matter in a CT image.

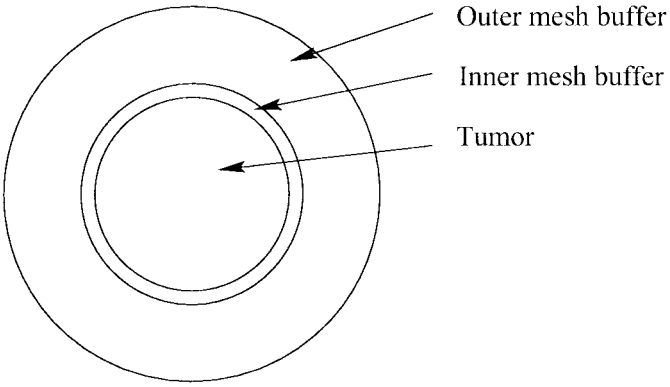

Fig. 1. A simple schematic of the tumor region. The inner circle represents the tumor. All nodes inside and on the boundary of the tumor are given the expansion strain. In effect, the inner mesh buffer (area between the first and second circles) elements that have common nodes with the tumor receive some expansion as well so, by design, this circular region is small. The outer mesh buffer is a rather large one and is used with a low-mesh-density factor to allow for radially long and narrow elements that would better absorb the high distortion of the expansion phase.

B. Tumor-Growth Mechanics

The mechanics of the tumor growth are complicated and by no means well understood (see [20], and references therein). As a first approximation, we have assumed that the tumor has the tendency to grow uniformly. Fig. 3(b) shows such an example. We have implemented this uniform growth model by defining a stress free configuration for the tumor seed to be the one which has a uniform strain e_0 [compare to (6)] applied to the seed. For a circular seed of D_s diameter, the grown tumor diameter D_t would tend to be $D_t = D_s(e_0 + 1)$. Thus, e_0 may be considered to be a growth factor. For example, if e_0 is zero, then there is no growth of the tumor seed, but if e_0 is one, the grown tumor would have a diameter twice that of the seed if it was free to expand. Since the tumor is elastically constrained by the stresses exerted by the surrounding brain tissue, it will tend to expand to a diameter less than $2D_s$ and the resulting growth of the tumor will tend to be nonuniform. The equilibrium equations in the form of the virtual work principle (7) govern the grown tumor size and shape. Note that if negative values of e_0 are applied to a tumor, it will contract, as described in Section II-E1.

C. Geometry, Boundary Conditions, and Mesh Generation

An MR/CT slice that contains the tumor is extracted from the volumetric brain image. The boundaries of the brain parenchyma and of the ventricles are then defined as sequences of points (see Fig. 2), either manually or via an active contour algorithm [25]. These boundary representations are then used by the quadratic mesh generator (QMG), a geometric modeler and automatic mesh generator developed by Vavasis [26]. QMG results in a triangular mesh, like the one shown in Fig. 5(b).

The tumor is meshed in the same way. As we described in Section II-B, a uniform strain is applied within the tumor, resulting in its growth. Since in the ABAQUS FEM platform

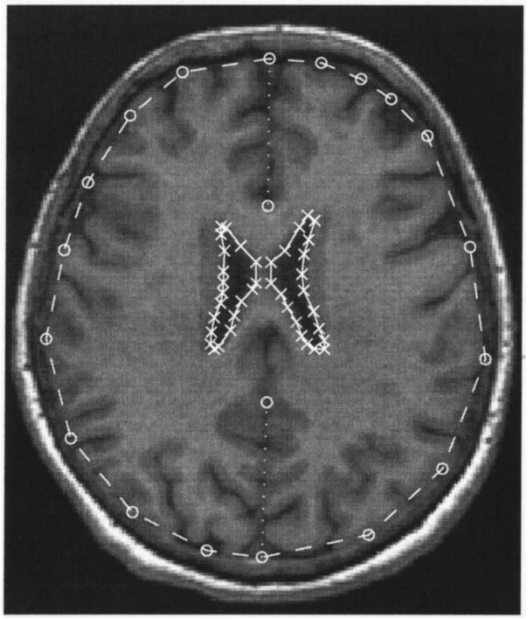

Fig. 2. Extraction of data from an MR slice. Data are manually digitized. Crosses represent points on the ventricles and circles represent points on the dura and falx. The dashed piecewise linear boundary represents the dura and is currently restrained from moving. The same holds for the two dotted lines that represent the falx. The ventricles are depicted with solid lines and are separated by the septum. They are assumed to have zero pressure internally.

the strain can be prescribed only on nodes and not on elements, we use a rim of small triangular elements around the tumor in order to ensure that no expansion or contraction is applied to normal brain tissue (see, also, Section II-H).

The dura mater (the tough membrane that encloses the parenchyma), as well as the falx and tentorium, are assumed to be rigid and with no relative motion between them and the parenchyma (brain) at the contact surface. In addition, ventricular pressure is assumed to be zero. The various boundary conditions are automatically assigned to finite-element nodes through the use of the geometric modeler features of QMG. Contact surfaces are also set up at the ventricular boundaries wherever there seems to be contact from juxtaposed ventricular boundary regions.

D. Governing Equations

The mechanics of tumor growth are governed by the equilibrium equations which give rise to the virtual work principle; a formulation that is particularly suitable for finite-element solutions. In our case, since there are no surface forces or acceleration terms, the virtual work principle can be written as

$$\int_V \delta w \, dV = 0. \tag{7}$$

Here, δw is the change in stain energy w [given by (1)] due to a virtual displacement and V is the undeformed volume (see for example [27], p. 27). By introducing a uniform strain inside the tumor, the overall strain energy is increased. Subsequently, the tissue moves to a lower energy position, which is defined by the above equation. The problem is solved numerically, through the finite-element method, with the resulting nonlinear system of equations solved iteratively via some variation of the Newton–Raphson method. The output is the deformation of the tissue due to the tumor growth.

E. Estimating the Deformed Atlas

The previous subsections discussed the principles of biomechanical modeling of brain tissue. The modeling is needed for estimating the deformed atlas which is accomplished through the following steps.

1) The biomechanical model contracts the tumor in the patient images to, ideally, an infinitesimal mass, in order to create a normal brain image. This is a simple estimate of the anatomy prior to the tumor growth. Details are given in Section II-E1.
2) This step is not used in our experiments in this paper, but is included here for completeness. In particular, the resulting normal image can be corrected, based on shape statistics of the normal brain collected from a training set. Statistical shape models, such as the point distribution method [28], would be applicable here. We performed a simulated experiment in order to demonstrate why this step might be useful. As shown in Fig. 3, we started with an MR image of a normal individual, as shown in Fig. 3(a), and we simulated the tumor expansion, as shown in Fig. 3(b). The applied uniform expansion strain was larger than we used elsewhere. We then applied the contraction method, which yielded a rather unrealistic estimate of the normal anatomy, as shown in Fig. 3(c). Such an estimate could be further corrected, either using statistical shape estimation methods or using manual correction, as shown in Fig. 3(d). In the experiments in this paper, we have not performed this correction step. However, we are planning to investigate the importance of this step in our future work.
3) At this stage, a normal brain atlas is matched to this estimate of the previous step via a deformable registration method [29], [30].
4) A nonlinear regression scheme estimates the tumor's origin and volumetric expansion that best agrees with the observed deformed anatomy. In each iteration, the process of tumor growth estimation is applied to the atlas, resulting in the displacement of the surrounding structures and the transfer of the anatomical labels of the atlas to the patient's brain. Details are given in Section II-E2.

1) Simulation of Tumor Contraction: The reduction of the tumor to an infinitesimal mass is achieved via a uniform contraction model. We note here that, in practice, we only apply a partial contraction of the tumor, for two reasons. First, numerical instabilities, which might arise when extreme deformations of the finite-element mesh are present, limit the extent of the tumor contraction. Second, in reality, part of the tumor is brain tissue that has been invaded and not simply displaced by the tumor. This paper does not address the very complicated issue of estimating how much tissue was invaded and how much of it was displaced. This is one of our future goals.

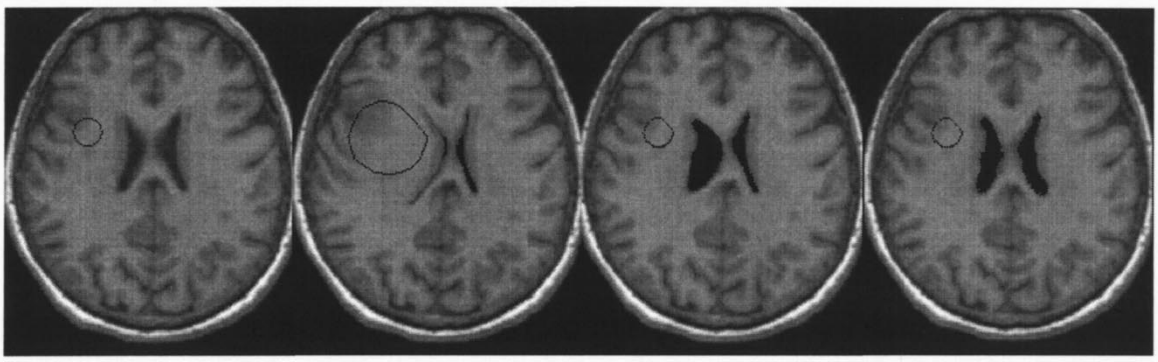

(a) (b) (c) (d)

Fig. 3. A demonstration of the limitations of the relatively simpler contraction method, and corrections to the contraction results. The growth of a tumor (a) was simulated based on a normal MR image (b). The tumor was then contracted, but the unrealistic deformation of (c) was obtained. This is because the brain with the tumor is in a strained condition, which is ignored during a simple contraction of the tumor (since, in reality, this strain would be unknown). (d) The image shows a correction obtained by manually outlining points along the ventricular boundaries and using these outlines in conjunction with the elastic warping to correct the image. This corrected image can now be used in a normal-to-normal atlas-matching procedure, followed by the simulation of the tumor growth via the nonlinear regression scheme, described in the paper.

If the stress distribution within a brain with a tumor (as well as the growth model) were known, then the process of tumor growth could be precisely reversed by relaxing the stress applied by the tumor and letting the normal tissue return to its undeformed state. However, this is not the case in reality. Therefore, we have to rely on certain assumptions, which in our model are the following: 1) zero initial stress throughout the brain and 2) a free strain within the tumor, which causes a uniform contraction. By free strain, here we mean that we would get this strain only if the material was completely free to contract. In our case, the resulting strain will also depend on the stiffness of the surrounding environment, as well as the mechanical properties of the tumor itself. In order to model the contraction of the tumor, the sign of the strain term e_0 is negative. Typically, we use values of e_0 in the range -0.6 to -0.9, inside the tumor, which tends to reduce its average diameter to approximately two fifths to one tenth of the original size.

2) Nonlinear Regression: In principle, the transformation resulting from the contraction of the tumor can be inverted, yielding the transformation describing the growth of the tumor. This would provide an approximate solution. However, such an approach would have certain drawbacks. One drawback stems from the fact that the brain is assumed to have zero stress in its tumor-bearing state. Therefore, unrealistic estimates of the patient's undeformed anatomy can be obtained during the tumor contraction process, as shown schematically in Fig. 3.

Thus, we have developed a method for directly modeling the expansion of the tumor, which we describe in this section. We are particularly concerned with determining two parameters: the origin of the tumor and the level of strain, e_0, that is required for the tumor expansion. We determine these optimal parameters via a nonlinear regression method. What drives this nonlinear regression scheme is a number of distinct anatomical features. In the experiments herein, we have used points along the boundaries of the tumor and the ventricles. However, features such as the sulci and the boundaries of subcortical structures can also be incorporated. The optimal set of parameters (tumor position and expansion strain) is the one which results in a deformation of the patient's brain that is most similar to the one that has been observed on the set of points mentioned above. Fig. 4 is a schematic of the regression process and shows how the difference in the computed versus experimental shapes of the ventricles and the tumor is used to drive the minimization process.

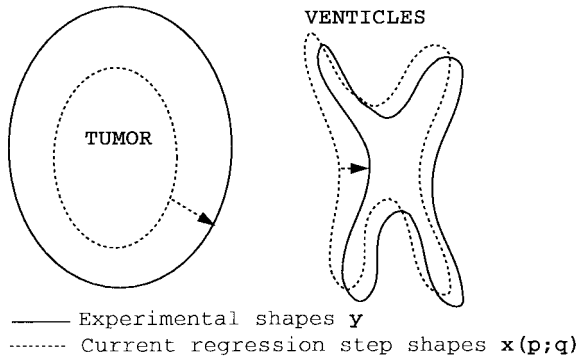

Fig. 4. At each regression step, computational results are compared to the tumor and ventricles (experimental) shapes in the patient image. The error between these shapes is minimized through the regression process, using sample points defined on the boundaries of the tumor, the ventricles, and the brain parenchyma. The variables $\boldsymbol{y}, \boldsymbol{p}$ and $\boldsymbol{x}$ are vectors of these point coordinates in the original patient images, the corresponding pre-tumor coordinates, and the corresponding (computed in current step) deformed coordinates, respectively. The vector $\boldsymbol{q}$ holds the parameters to be optimized.

The nonlinear regression is implemented using ABAQUS and the Marquardt algorithm [31], [32]. The Marquardt algorithm is used for the least squares estimation of nonlinear parameters. It performs the estimation by using an optimum interpolation between the steepest descent (gradient) and the Taylor-series methods. The interpolation is based upon the maximum neighborhood in which the truncated Taylor series gives an adequate representation of the nonlinear model. Thus, it overcomes the slow convergence of the steepest-descent method and the divergence of successive iterates of the Taylor-series method. Our Marquardt implementation is based on a public domain program by Shrager *et al.* [33].

Consider a number of points $\boldsymbol{y}_1 \cdots \boldsymbol{y}_N$, defined on the boundaries of the tumor, the ventricles, and the brain

parenchyma in the patient's images (deformed anatomy). Additional points identified on anatomical features, such as sulci and gyri, can also be included. Let the position of these points in the estimate of the patient's undeformed brain be $\boldsymbol{p}_1, \cdots, \boldsymbol{p}_N$. These points lie on the patient's images resulting from the tumor contraction and whatever further correction is applied. Let, also, $\boldsymbol{q}$ be a parameter vector, i.e., a vector holding the values of the x and y coordinates of the tumor origin and the value c_0 of the tumor strain parameter. Finally, let $\boldsymbol{x}(\boldsymbol{p};\boldsymbol{q})$ be the position to which a point $\boldsymbol{p}$ in the patient's undeformed images is mapped to, via the tumor growth transformation that depends on the parameter vector $\boldsymbol{q}$. Our objective is to find the parameter vector $\boldsymbol{q}$ that minimizes the following objective function:

$$f(\boldsymbol{q}) = \frac{1}{N} \sum_{i=1}^{N} ||\boldsymbol{x}(\boldsymbol{p}_i;\boldsymbol{q}) - \boldsymbol{y}_i||^2. \tag{8}$$

Our initial estimate for $\boldsymbol{q}$ consists of the coordinates of the center of area of the contracted tumor and of an expansion strain value c_0, which may be determined from the size of the tumor. During each iteration, $\boldsymbol{q}$ is updated by the Marquardt method. However, certain limits are placed on the maximum allowable steps for each of the three parameters in $\boldsymbol{q}$. Currently, all three parameters are only allowed to have a maximum relative change of 0.5. This precludes large steps in the parameter values that might throw off either the automated meshing for the case of the x and y centroid coordinates, or the rather sensitive nonlinear solution for the case of the expansion strain. When a new value of $\boldsymbol{q}$ is determined, the finite-element module is called to update the transformation $\boldsymbol{x}(\cdot)$ and hence reevaluate the objective function $f(\boldsymbol{q})$ and the gradient of $f(\boldsymbol{q})$. Clearly, this is a very costly procedure. For this reason, in our current work we have used only three parameters for $\boldsymbol{q}$**.** Our method, however, can be applied more generally, depending on the available time frame and computational machinery.

Application of the routine is straightforward with one exception. The value of the parameter increases that are used by the regression for finding the numerical Jacobian with a forward differences method must be large enough to accommodate the approximate nature of the finite-element solution. This is especially true in our case where the finite-element mesh may be different in each iteration, due to some idiosyncrasies of the meshing software QMG. Merely a change in the finite-element mesh may produce some change in the deformations, even though no other parameters have been changed. An increase equal to the product of an empirical constant 0.01, multiplied by the value of the parameter, was found sufficient to produce good results in our work.

F. Reconstruction of the Deformed Image

The solution to the procedure described in the previous section is a deformation vector field $\boldsymbol{x}(\cdot)$. We then form a deformed image via an interpolation scheme, as explained next. First, we scale the finite-element data to the original image size, to facilitate image creation. For each deformed finite element, we create a grid with subdivisions no larger than the pixel resolution of the image. For each grid point, we use standard finite-element shape functions to calculate both the undeformed and deformed points that correspond to it. The final step is to give the intensity of the nearest undeformed pixel to the corresponding nearest deformed pixel. In this way, we produce a deformed image that corresponds to the finite-element deformation, applied to the undeformed image.

G. Finite-Element Convergence Study

The convergence of the finite-element solution is tested as follows [34]. A rather coarse mesh is first created with approximately 150 nodes. The mesh is then refined by subdividing each element into four smaller elements. The same procedure is repeated one more time, to produce a total of three meshes of increasing density. The nodal values for the displacement solutions, given by the three meshes, are then compared to estimate model accuracy and convergence. The displacement vector $\boldsymbol{u}_{\text{fine}}$ (written as a long vector $[x_1, y_1, x_2, y_2, \cdots, x_N, y_N]$, N being the number of nodes) from the finest mesh is considered correct and each of the other two displacement vectors $\boldsymbol{u}_{\text{coarse}}$ is compared to it to calculate the error vector $\boldsymbol{E}_{\text{error}}$:

$$\boldsymbol{E}_{\text{error}} = \boldsymbol{u}_{\text{fine}} - \boldsymbol{u}_{\text{coarse}}. \tag{9}$$

The root mean square of this error vector gives a discrete measure of the L_2 error norm E_{L_2} for the coarse element mesh

$$E_{L_2} = \sqrt{\frac{\boldsymbol{E}_{\text{error}} \cdot \boldsymbol{E}_{\text{error}}}{N_E}} \tag{10}$$

where N_E is the size of the vector $\boldsymbol{E}_{\text{error}}$. We then plot the results in a logarithmic scale to observe the convergence rate.

H. The Tumor Region

For the tumor expansion part we use a higher mesh density in the tumor region, compared to the rest of the brain tissue, since we expect large deformations in that region. We also have to deal with two more problems in that area. First, to avoid problems with elements next to the tumor being overly distorted, we force our mesh generator to produce elements of a radially longer size by creating the outer mesh buffer, an extra region around the tumor that is assigned a relatively low mesh density (see Fig. 1). Second, we create the inner mesh buffer, a region smaller than the outer mesh buffer region, also enclosing the tumor, which helps avoid having large elements next to the tumor boundary. For technical reasons, the strain was applied as a nodal variable rather than an element variable. Thus, by applying the strain on the nodes on the interior, as well as on the boundary of the tumor area, we inadvertently apply the same strain on parts of the elements that surround the tumor and have common nodes with the boundary. Therefore, in the case that these elements happen to be large in size, that would indicate that we have applied the expansion on a larger area than we had intended. To reduce this problem, we create a slightly enlarged area with a fixed radius of usually 1.1 times the radius of the tumor with appropriate mesh size properties, in order to have small elements in that area.

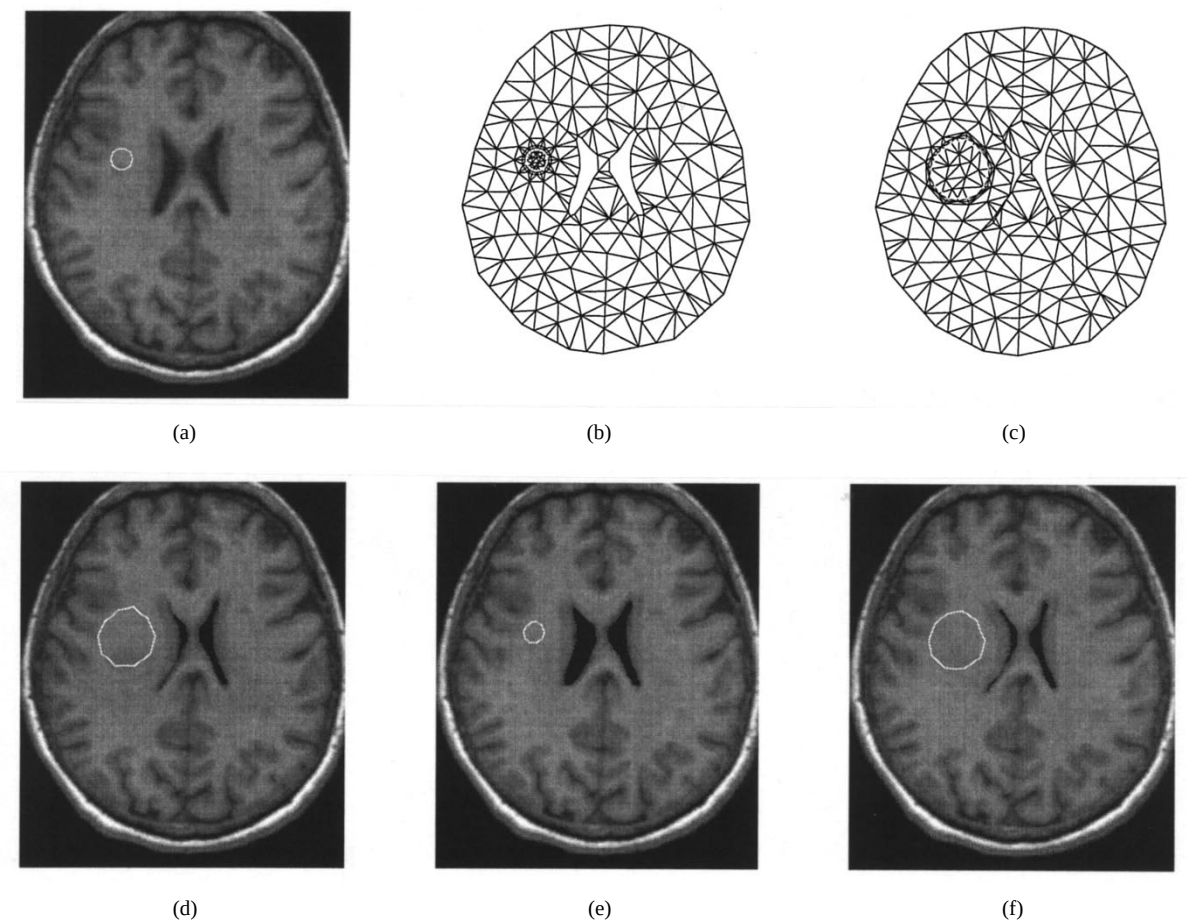

Fig. 5. A simulated tumor case. (a) The original image with the simulated tumor seed. (b) The finite-element mesh. (C) The deformed mesh due to a uniform expansion of the tumor seed to approximately three times the original diameter. (D) The deformed image recreated, as explained in Section II-F. (E) The contracted image (by a uniform strain of -0.66). (F) The image produced by the nonlinear regression results.

III. Results

In our first experiment we tested our algorithm on simulated images. In particular, we placed a tumor seed in a normal MR image [Fig. 5(a)], and we applied our expansion model to create an MR image with a tumor [Fig. 5(d)]. The size of the tumor seed (about 1-cm diameter) was such that a reasonably sized tumor could be simulated by seed expansion, without the need for finite-element remeshing. The expansion strain was four. Contact elements were placed in the right lateral ventricle (left in the image), in order to avoid self intersections. After the data extraction and mesh creation phase, explained in Section II-C, a mesh is obtained. We refer the reader to panel (b) of Fig. 5 [Fig. 5(b)]. By running ABAQUS with the loads, material properties, and boundary conditions, we obtained the deformed configuration shown in Fig. 5(c). As explained in Section II-F, application of the finite-element deformation map to the original image of Fig 5(a), allowed us to reconstruct the deformed image depicted in Fig. 5(d). The simulated tumor of Fig 5(d) was then treated as the starting point for applying the contraction part described in Section II-E1. Fig. 5e was produced after we applied a contraction strain of -0.66, by trial and error, so that the resulting contracted tumor had a size within a 2% relative error of the original tumor seed of Fig. 5(a). Ideally, the difference between Fig. 5(e) and (a) should be as small as possible. Fig. 5(f) is created by application of the results from the nonlinear regression to the contracted image of Fig. 5(e). There is a good agreement between Fig. 5(d) and (f), which indicates that our model behaves as expected.

As we mentioned earlier, the primary reason for first simulating a tumor growth, rather than using a patient tumor image, was to actually test our method since we knew the exact position of the original tumor seed [Fig. 5(b)]. This testing is shown in Fig. 6, which displays the seed and tumor configurations for the true, as well as the contraction and regression, results. Only the area around the tumor and ventricles is shown for clarity. In particular, the solid lines represent the true configuration, the dashed lines represent the contraction results, and the dotted lines represent the regression results. The smaller circular region on the left is the tumor seed, while the larger one is the tumor. Note that both the estimated tumor seed (dotted) as well as the contraction tumor seed are very near the true tumor seed (solid line).

Table I gives representative results for the simulated regression case. We observe a very good agreement between the true and the estimated parameters. The guess for the x and y coordinates is based on the contraction results, which seem to give a very good guess as to these parameters. The expansion strain true value of 2.4 was estimated to be 2.42, with a guess of 0.6.

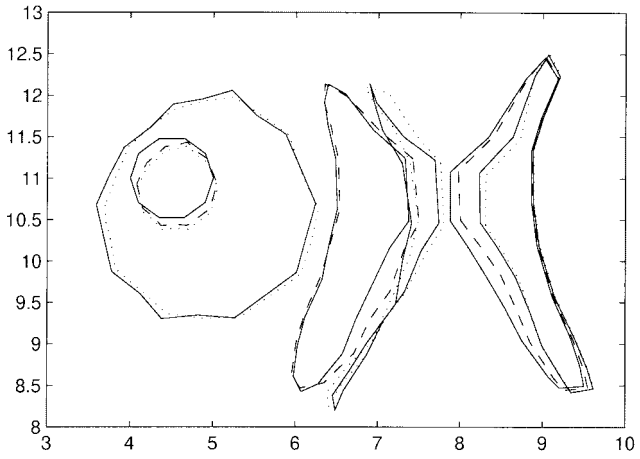

Fig. 6. Comparison of normalization results by using the contraction part alone versus the addition of the regression part. Shown are the tumor seed and tumor (small and large approximately circular shapes on our left) and the ventricles (on our right) in their pre-tumor and tumor state. The contraction results are shown in dashed lines, while the regression results are shown in dotted lines. The simulated experimental data are in solid lines. Note that, as explained in Section II-E2, the pre-tumor ventricle state is the same for both the contracted and regression parts.

TABLE I
REGRESSION RESULTS FOR THE SIMULATION EXAMPLE OF FIG. 5. THE THREE PARAMETERS ARE THE x AND y COORDINATES OF THE TUMOR SEED CENTER AND THE EXPANSION FACTOR

	X Coord (cm)	Y Coord (cm)	Expansion Strain
True	4.5	11	2.4
Guess	4.56	10.91	0.6
Estimated	4.57	10.86	2.42

In our second experiment, we demonstrated our tumor growth model on two MR images from a patient who underwent radiation therapy that almost eliminated the metastatic tumor, as shown in Fig. 7(a) and (b). Fig. 7(a) is the image before the irradiation, with the tumor visible in the right (left in the image, according to the radiology convention) caudate nucleus. Fig. 7(b) shows images of the same patient six months after irradiation, with only remnants of the tumor visible. Note that the volume containing this image was rigidly registered (through use of the automatic image registration (AIR) package [35]) to the volume of Fig. 7(a). The image of Fig. 7(b) was extracted from the same level of the brain as in Fig. 7(a). Fig. 7(c) is the contracted image of Fig. 7(a), after applying the uniform tumor contraction. The tumor-seed estimate is shown as a small outline. In addition to the tumor contraction, in this experiment we applied a uniform contraction to the edema that had formed around the tumor. The edema was determined from the T_2-weighted images of the same patient. Fig. 7(d) shows the T_2-weighted image, in which the edema appears relatively brighter. In contracting the edema, we used a 20% uniform volume contraction. This value was chosen to be approximately in the middle of the range from 10 to 40%, since edema is known to result in a 10–40% volumetric expansion.

In order to compare our estimate of the patient's brain after the contraction of the tumor, as shown in Fig. 7(a), with the truth, as shown in Fig. 7(b), we selected eight landmark points, located at the center of the crosses. We defined these landmarks in Fig. 7(a)–(c), and we then measured the Euclidean distance between corresponding pairs of landmarks. The sizes of the crosses are proportional to the distance between the corresponding landmarks in each location. For reference, we have added a cross at the bottom right of the images, which represents a distance of 4 mm. A comparison between Fig. 7(a) and (c) reveals a considerable reduction in the landmarks' distance, as expected. The actual values of the distances recorded on these landmarks for Fig. 7(a) and (c) are shown in Table II. Note that, in addition to landmarks situated near the tumor, we selected two landmarks that are far away, in order to demonstrate that part of the landmark distances observed is due to the rigid registration between these images and to human error in defining these landmarks.

Figs. 8 and 9 represent results of applying the contraction and subsequent regression to an actual patient tumor-bearing CT image and to the related atlas images. Fig. 8 gives the contraction results. Fig. 8(a) shows the patient image with a white outline denoting the tumor. Fig. 8(b) is the corresponding finite-element mesh. Fig. 8(c) is the pre-tumor mesh after the application of a contraction strain of -0.60, which reduces the size (area) of the tumor by approximately four times. Fig. 8(d) is the superposition of the deformation mapping on the original image.

Fig. 9 displays the atlas-matching results for the same patient. Fig 9(a) is the original atlas, obtained from [36] after digitization performed in our laboratory. Fig. 9(b) presents the warped atlas using the method described in [30] and [29], by using the overall size of the brain and ventricles. Fig. 9(c) presents the image of Fig. 9(b), deformed by the simulated tumor growth (from regression) to obtain an atlas that has the characteristics of our patient tumor image. The vertical white lines in both Fig. 9(a) and (b) have been added to illustrate the deformations. Finally, Fig. 9(d) is the patient image with a few of the structures of the atlas in Fig. 9(c) superimposed. In particular, most of the thalamic structures, the putamen, the claustrum, the cortex, and the ventricles have been included.

As explained in the Methods section, to test the convergence of our finite-element simulations we plotted the L_2 error norm against the number of nodes on a logarithmic scale (Fig. 10). The problem on which we tested the convergence is the expansion part of the Fig. 5 case. The results show a slope of 0.9, which appears to be a reasonable convergence rate. From the figure we see that for about 600 nodes, the error is about 0.01, which means that for a 1-cm movement, an average error of 0.01 cm would be observed. Since in most of our simulations the number of nodes was more than 600, we conclude that the finite-element accuracy is appropriate for our purposes.

IV. DISCUSSION

We presented a framework for modeling the deformations applied to brain tissue by a growing tumor. The main

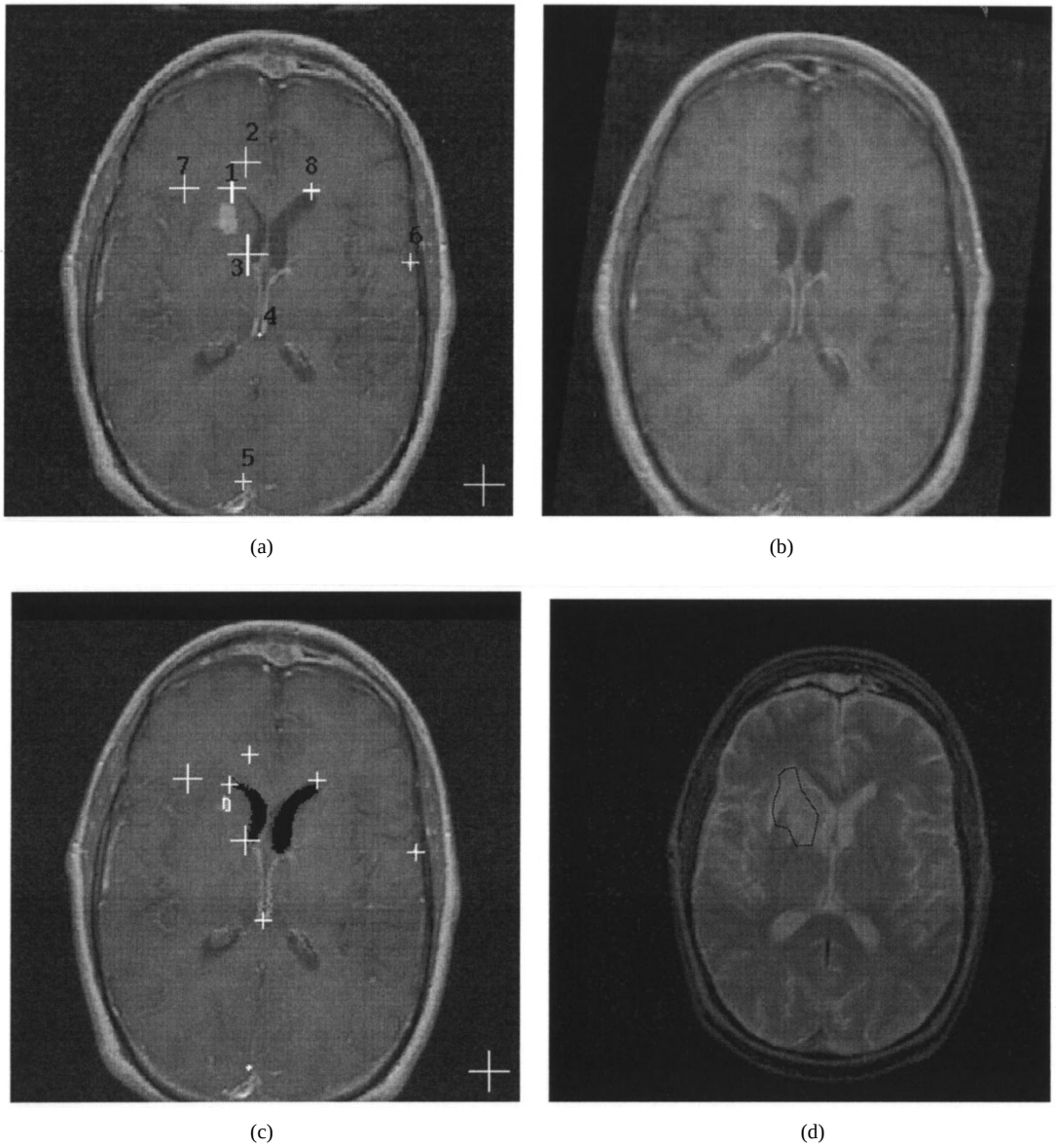

Fig. 7. Verification using time series data. (a) Axial MR image with tumor intact. (b) Same patient image at a later time after tumor radiosurgery has shrunk the tumor. (c) Our regression pre-tumor image. The crosses in (a) and (c) represent the distance in eight landmark registration between (a) and (b) and (c) and (b). The error includes registration error and human error. Note that, overall, most crosses in (c) are smaller, which indicates that our regression results improve the registration process. Crosses in the lower right corners represent an error of 4 mm. An initial 20% (-0.2) strain uniform reduction of the edema was applied to the edematous region seen in the T_2 weighted image of (d) (dark outline).

TABLE II
DISTANCES (mm) IN THE EIGHT LANDMARKS BETWEEN PANEL B [FIG. 7(b)] AND PANELS A [FIG. 7(a)] AND C [FIG. 7(c)]. MEAN DISTANCES ARE 2.1 mm FOR PANEL A AND 1.4 mm FOR PANEL C, AN INDICATION THAT THE NORMALIZATION PROCESS IMPROVES REGISTRATION

Panel A	2.8	2.5	3.5	0.0	1.6	1.7	2.8	1.7
Panel C	1.1	1.7	2.3	1.1	0.8	1.1	2.2	1.1

application is in the deformable registration of anatomical atlases with images from patients with tumors, which facilitates the surgical or radiosurgical planning. At this stage of our work, we have focused primarily on the modeling of the nonlinearity in the elastic behavior of soft tissue, as well as its inhomogeneity; on constraints imposed by the skull, the tentorium, and the falx; and on the ventricular deformations caused by tumors. Tumor growth has been based on a uniform volumetric expansion, restrained by the surrounding anatomy.

Our framework for adapting a normal atlas to a brain with a tumor can be thought of as a four-step procedure. First, a rough estimate of the brain in its original, undeformed state is obtained by contracting the tumor to (ideally) an infinitesimal mass. In the second step, which is included here for completeness but not yet used, a correction will be applied to the results from the first step. In the third step, a normal-to-normal deformable registration method is used. Finally, in the fourth step, a regression scheme is employed to model the tumor growth on the labeled patient image, which results in the deformation of the atlas-labeled anatomy and, therefore, to a labeling of the patient's deformed anatomy.

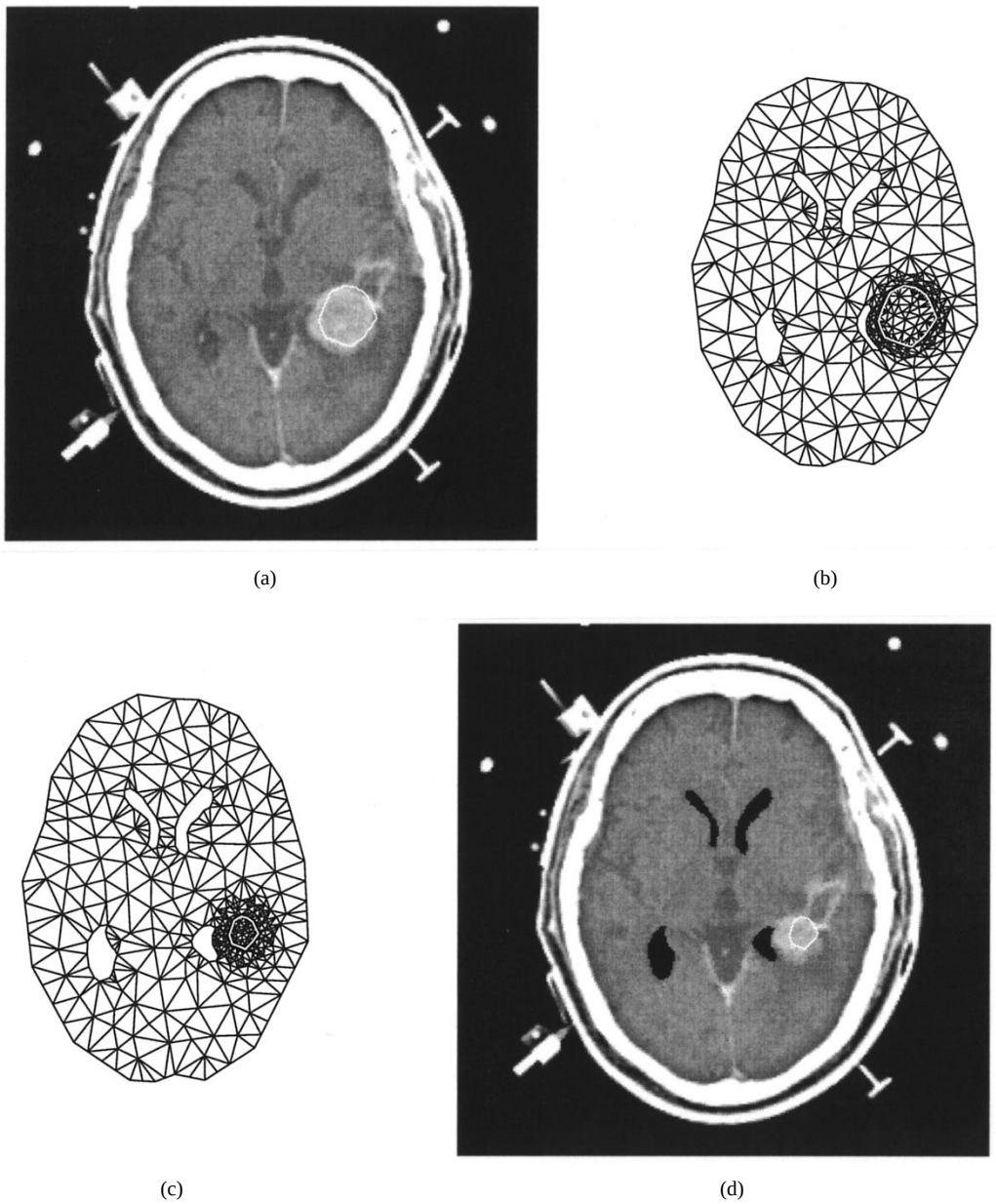

Fig. 8. Contraction results for an actual tumor: CT image from a patient (a) with the tumor highlighted. (b) and (c) show the undeformed and deformed finite-element meshes. (d) The image created by deforming the image in panel A based on the finite-element mapping. Note that the slight mismatch between the tumor and its outline in (a) was needed to combat imperfections in our automatic mesh generation scheme, due to the ventricle being very near the tumor.

The contraction of the tumor in the first step of this procedure is described by a transformation. In principle, one could apply the inverse transformation in order to obtain the tumor expansion. However, there are certain limitations in that approach, which were outlined in Section II-E2. Most importantly, the lack of knowledge of the residual stresses caused by the tumor growth often results in poor estimates of the patient's anatomy prior to the growth of the tumor. The nonlinear regression scheme provides a way of remedying this limitation in the future, by incorporating into the estimation procedure and, in particular, in the vector $\boldsymbol{q}$, shape parameters in addition to the tumor position and growth parameters which we currently use. Therefore, it is a much richer method, although it comes at the cost of increased computational requirements.

Our model for tumor growth has two limitations. The first stems from the fact that the tendency of the tumor to grow might actually be influenced by the surrounding stresses exerted by brain tissue. We note that in our current scheme, there is a tendency for a uniform tumor growth. However, the final tumor shape is not spherical, due to the surrounding constraining stresses. However, it could be the case that the tumor cells have the tendency to grow along minimal stress directions. Currently, there is insufficient knowledge of exactly how the tumor growth is affected by surrounding stresses. However, when such knowledge becomes available, it could be incorporated into our model. The second limitation stems from the fact that we have not accounted for tumor infiltration. An infiltrating tumor does not push away the brain tissue, which is one of our fundamental assumptions in modeling the

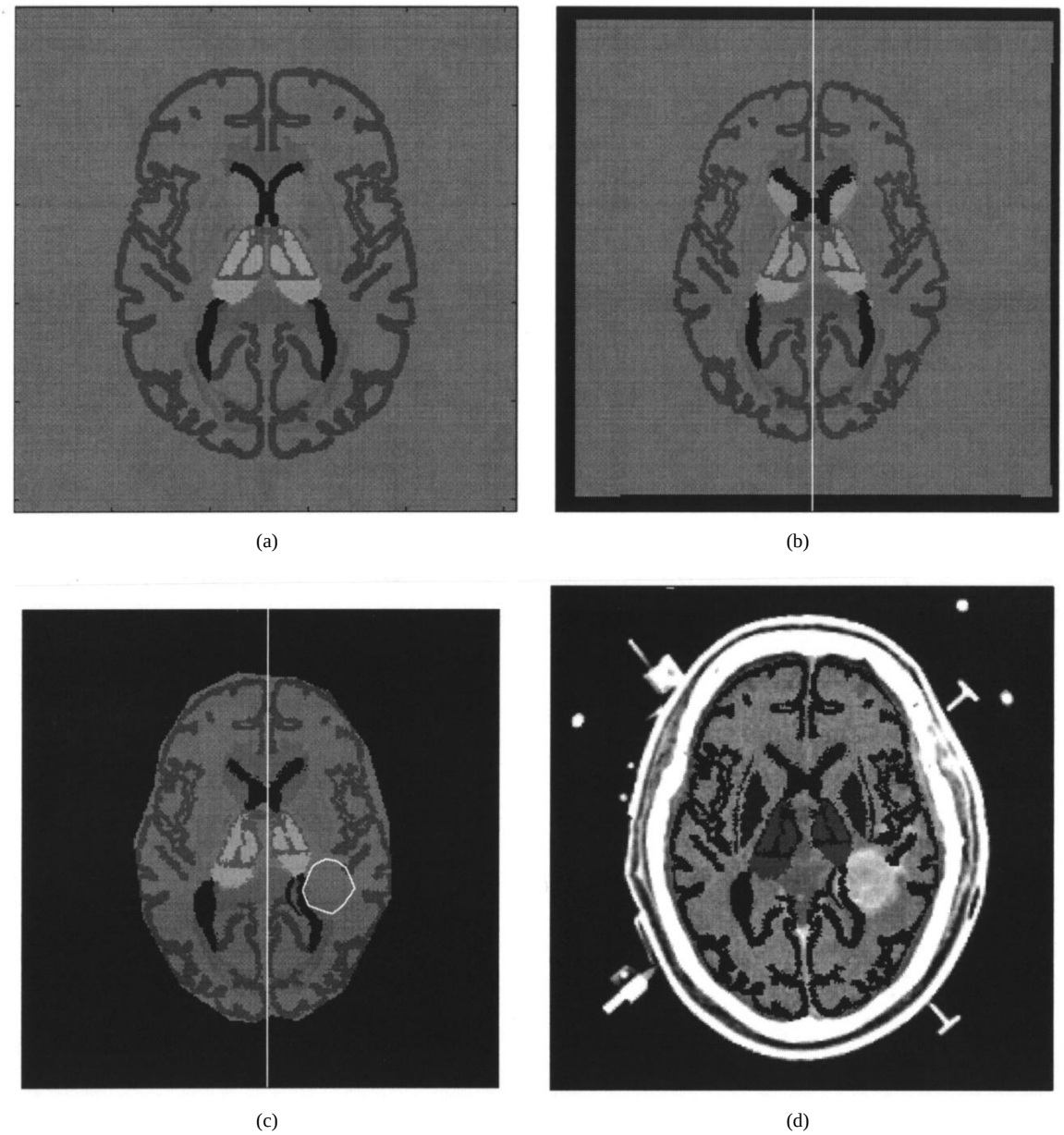

Fig. 9. Regression results for an actual tumor—atlas manipulations. (a) The original atlas slice. (b) The atlas slice warped in overall registration with the patient's image. (c) The deformation of the atlas in (b), based on the regression results of the experiment in Fig. 8. The white outline represents the position of the tumor in the patient's image. (d) Here we have superimposed some of the atlas structures from the deformed atlas of (c) on the image of Fig. 8(a). (b) and (c) have been enhanced with the addition of a vertical white line to better visualize the midline shift changes.

deformation imposed by the tumor growth. In our future work we plan to use the assumption that the tumor is comprised of two parts, one which infiltrates and one that pushes away brain tissue. Under simplifying assumptions, these regions could be estimated within the regression framework.

In our demonstration experiment, which was based on tumor recession after radiotherapy, we modeled the expansion due to edema based only on rough estimates of volumetric expansion taken from the literature. A more accurate modeling could be achieved by including the degree of volumetric expansion of the edematous region as an additional parameter of the vector $\boldsymbol{q}$, to be estimated in the nonlinear regression scheme. More sophisticated modeling of edema using poroelastic [18], [13] material behavior may be of some advantage. However, at this point it is unclear if that is the case for our particular application, especially in view of the much higher computational requirements of such models.

One of the limitations in the practical implementation of the algorithm is that the tumor growth cannot exceed certain limits. This is due to numerical instabilities of the finite-element model arising when the elements become very distorted (especially around the tumor). In future work we plan to introduce remeshing techniques, which will recreate the finite-element mesh after a certain level of distortion.

Extension of these methods to 3-D will better model the brain tissue deformation caused by a growing tumor, since it will account for out-of-plane deformations, which cannot be handled by our current 2-D model. There are several

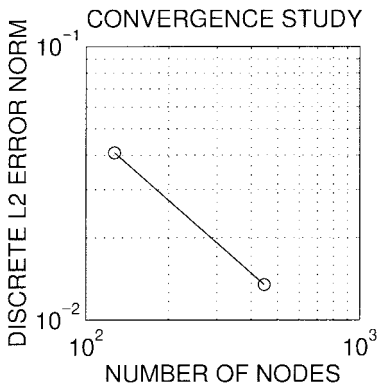

Fig. 10. Convergence study of our finite-element mesh. Plot of the discrete L_2 error norm against the number of nodes for successively finer meshes. The slope of the log/log plot is approximately 0.9 (negative) which is in a reasonable range, indicating good convergence of our solutions.

major challenges in 3-D. Most importantly, the computational requirements rise exponentially, more sophisticated meshing algorithms are needed, and the visualization of the results becomes difficult.

The inclusion of different material properties for the gray and white matter was done automatically by assigning each finite element a stiffness, calculated from the value of the pixel at the element centroid, as a first approximation. This assumes that intensities for gray and white matter are easily differentiated, which is the case for MRI. In addition, the tumor tissue is often considerably harder than the rest of the brain tissue. Unfortunately, we are not aware of any quantitative studies of the elastic properties of tumor tissue, and we have resorted to arbitrarily using the material properties of gray matter.

We have run all our computations on an SGI Onyx, using one of its R10000 processors and 1 Gb of RAM. The contraction case runs in about 30 s to 2–3 min, depending mostly on the number of nodes. In contrast, the regression case is very computationally intensive since it requires the repeated finite-element solution that, depending on the guess, may range from about 15 finite-element analysis calls (around 15 min if 1 min per call) to more than 100 (100 min). The CPU requirements are expected to become much higher for the 3-D implementation. In our 2-D examples the improvement in estimation from the regression part was very small compared to the estimation from the contraction part. If the same effect is observed in our 3-D models, we might have to accept the less sophisticated contraction in favor of its lower computational demands.

In summary, we have shown the utility of a biomechanical FEM model as a means of modeling soft tissue deformation, and its application to the problem of deformable atlas registration. The technique has the potential to be used in several forms of pre-operative planning.

ACKNOWLEDGMENT

The authors like to thank Dr. D. Long, Department of Neurosurgery, The Johns Hopkins Hospital, Dr. K. Costa, Washington University, St. Louis, MO, Dr. J. Humphrey, Texas A&M University, and Dr. S. Neff, Wills Eye Hospital, Philadelphia, PA, for many helpful discussions, and Dr. J. Williams, Department of Neurosurgery, The Johns Hopkins Hospital, for providing some of the images and for his valuable feedback regarding the applicability of these methods to radiosurgical planning.

REFERENCES

[1] M. I. Miller, G. E. Christensen, Y. Amit, and U. Grenander, "Mathematical textbook of deformable neuroanatomies," *Proc. Nat. Acad. Sci.*, vol. 90, pp. 11944–11948, 1993.

[2] C. Davatzikos, M. Vaillant, S. Resnick, J. L. Prince, S. Letovsky, and R. N. Bryan, "A computerized approach for morphological analysis of the corpus callosum," *J. Comput. Assist. Tomogr.*, vol. 20, pp. 88–97, Jan./Feb. 1996.

[3] G. Subsol, J. P. Thirion, and N. Ayache, "Application of an automatically built 3-D morphometric brain atlas: Study of cerebral ventricle shape," *Vis. Biom. Comp., Lecture Notes Comp. Sci.*, 1996, pp. 373–382.

[4] M. Vaillant, C. Davatzikos, R. H. Taylor, and R. N. Bryan, "A path-planning algorithm for image guided neurosurgery," in *Proc. CVRMed II - MRCAS III*, Mar. 1997, pp. 467–476.

[5] J. Kaye, D. N. Metaxas, and F. P. Primiano, Jr., "A 3-D virtual environment for modeling mechanical cardiopulmonary interactions," *CVRMed-MRCAS'97 Lecture Notes in Computer Science*, 1997.

[6] C. R. Maurer Jr., D. L. G. Hill, A. J. Martin, H. Liu, M. McCue, D. Rueckert, D. Lloret, W. A. Hall, R. E. Maxwell, D. J. Hawkes, and C. L. Truwit, "Investigation of intraoperative brain deformation using a 1.5-T interventional MR system: Preliminary results," *IEEE Trans. Med. Imag.*, vol. 17, pp. 817–25, Oct. 1998.

[7] K. D. Paulsen, M. I. Miga, F. E. Kennedy, P. J. Hoopes, A. Hartov, and D. W. Roberts, "A computational model for tracking subsurface tissue deformation during stereotactic neurosurgery," *IEEE Trans. Biomed. Eng.*, vol. 46, pp. 213–25, Feb. 1999.

[8] R. D. Bucholz, D. D. Yeh, J. Trobaugh, L. L. McDurmont, C. C Sturm, C. Baumann, J. M. Henderson, A. Levy, and P. Kessman, "The correction of stereotactic inaccuracy caused by brain shift using an intraoperative ultrasound device," *CVRMed-MRCAS'97 Lecture Notes in Computer Science*, 1997.

[9] M. Bro-Nielsen, "Surgery simulation using fast finite elements," in K. H. Hohne and R. Kikinis, Eds., *Visualization in Biomedical Computing*. Berlin, Germany: Springer-Verlag, 1996, pp. 529–34.

[10] H. Metz, J. McElhaney, and A. K. Ommaya, "A comparison of the elasticity of live, dead, and fixed brain tissue," *J. Biomech*, vol. 3, no. 4, pp. 453–458, 1970.

[11] S. N. Atluri, A. S. Kobayashi, and J. S. Cheng, "Brain tissue fragility—A finite strain analysis by a hybrid finite-element method," *ASME J. Appl. Mech.*, June 1975, pp. 269–273.

[12] F. A. Bandak, M. J. Vander Vorst, L. M. Stuhmiller, P. F. Mlakar, W. E. Chilton, and J. H. Stuhmiller, "An imaging-based computational and experimental study of skull fracture: Finite element model development, [Review] [31 refs]," *J. Neurotrauma*, vol. 12, no. 4, pp. 679–688, 1995.

[13] T. Nagashima, T. Shirakuni, and S. I. Rapoport, "A two-dimensional, finite element analysis of vasogenic brain edema.," *Neurologia Medico-Chirurgica*, vol. 30, no. 1, pp. 1–9, 1990.

[14] T. Nagashima, N. Tamaki, M. Takada, and Y. Tada, "Formation and resolution of brain edema associated with brain tumors. A comprehensive theoretical model and clinical analysis," *Acta Neurochir. Suppl.*, vol. 60, pp. 165–167, 1994.

[15] T. Nagashima, Y. Tada, S. Hamano, M. Skakakura, K. Masaoka, N. Tamaki, and S. Matsumoto, "The finite element analysis of brain oedema associated with intracranial meningiomas," *Acta Neurochir. Suppl.*, vol. 51, pp. 155–157, 1990.

[16] T. Nagashima, T. Shirakuni, and S. I. Rapoport, "A two-dimensional, finite element analysis of vasogenic brain edema," *Neurologia Medico-Chirurgica*, vol. 30, no. 1, pp. 1–9, 1990.

[17] T. Nagashima, N. Tamaki, S. Matsumoto, B. Horwitz, and Y. Seguchi, "Biomechanics of hydrocephalus: A new theoretical model," *Neurosurgery*, vol. 21, no. 6, pp. 898–904, 1987.

[18] R. P. Subramaniam, S. R. Neff, and P. Rahulkumar, "A numerical study of the biomechanics of structural neurologic diseases," in *Proc. High-Performance Computing—Grand Challenges Computer Simulation Society Computer Simulations*, San Diego, CA, 1995, pp. 552–560.

[19] H. Takizawa, K. Sugiura, M. Baba, and J. D. Miller, "Analysis of intracerebral hematoma shapes by numerical computer simulation using the finite element method," *Neurologia Medico-Chirurgica*, vol. 34, pp. 65–69, 1994.

[20] R. Wasserman and R. Acharya, "A patient-specific in vivo tumor model. [Review]," *Math. Biosci.*, vol. 136, no. 2, pp. 111–140, 1996.
[21] Abaqus version 5.5., Hibbit, Karlsson, and Sorensen, Inc., USA, 1995.
[22] M. E. Gurtin, *An Introduction to Continuum Mechanics*. Orlando, FL: Academic, 1981.
[23] K. K. Mendis, R. L. Stalnaker, and S. H. Advani, "A constitutive relationship for large deformation finite element modeling of brain tissue," *J. Biomech. Eng.*, vol. 117, no. 3, pp. 279–285, 1995.
[24] J. D. Humphrey, "Mechanics of the arterial wall: Review and directions. [Review] [512 refs]," *Critical Rev. Biomed. Eng.*, vol. 23, nos. 1–2, pp. 1–162, 1995.
[25] C. A. Davatzikos and J. L. Prince, "An active contour model for mapping the cortex," *IEEE Trans. Med. Imag.*, vol. 14, pp. 65–80, Mar. 1995.
[26] S. A. Vavasis, "QMG: A finite element mesh generation package." Available HTTP: http://www.cs.cornell.edu:/Info/People/vavasis/qmg-home.html, 1996.
[27] O. C. Zienkiewicz and R. L. Taylor, *The Finite Element Method*, 5th ed. London, U.K.: McGraw-Hill, 1988.
[28] F. T. Cootes and C. J. Taylor, "Combining point distribution models with shape models based on finite element analysis," *Image Vision Comput.*, vol. 13, no. 5, pp. 403–409, 1995.
[29] C. Davatzikos, "Spatial transformation and registration of brain images using elastically deformable models," *Comput. Vision Image Understanding*, vol. 66, no. 2, pp. 207–222, May 1997.
[30] ———, "Spatial normalization of 3-D images using deformable models," *J. Comput. Assist. Tomogr.*, vol. 20, pp. 656–665, July/Aug. 1996.
[31] D. W. Marquardt, "An algorithm for least-squares estimation of nonlinear parameters," *J. Soc. Indust. Appl. Math.*, vol. 11, p. 431, 1963.
[32] S. K. Kyriacou, A. D. Shah, and J. D. Humphrey, "Inverse finite element characterization of the behavior of nonlinear hyperelastic membranes," *ASME J. Appl. Mech.*, vol. 64, pp. 257–262, 1997.
[33] R. I. Shrager, A. Jutan, and R. Muzic. "Leasqr.m." Available FTP: ftp://ftp.mathworks.com: /pub/contrib/v4/optim/peakfit/leasqr.m, 1994.
[34] S. K. Kyriacou, C. Schwab, and J. D. Humphrey, "Finite element analysis of nonlinear orthotropic membranes," *Comput. Mech.*, vol. 18, pp. 269–278, 1996.
[35] R. P. Woods, J. C. Mazziotta, and S. R. Cherry, "MRI-PET registration with automated algorithm," *J. Comput. Assist. Tomogr.*, vol. 4, pp. 536–546, 1993.
[36] J. Talairach and P. Tournoux, *Co-planar Stereotaxic Atlas of the Human Brain*. Stuttgart, Germany: Thieme, 1988.